

Grain Boundary Defect Production during Successive Displacement Cascades on a Tungsten Surface

Yang Zhang¹, Predrag Krstic², and Jason R. Trelewicz^{1,2*}

¹Department of Materials Science and Chemical Engineering, Stony Brook University, Stony Brook, NY 11794

²Institute for Advanced Computational Science, Stony Brook University, Stony Brook, NY 11794

*Corresponding Author: jason.trelewicz@stonybrook.edu

Abstract

This study delves into the complex mechanisms of defect production and accumulation in nanocrystalline tungsten under irradiation, with a particular focus on the interplay between grain boundaries and free surfaces. Through molecular dynamics simulations, the research explores how grain boundaries act as sinks for irradiation-induced defects, a critical aspect in designing nanomaterials with enhanced radiation tolerance. The investigation leverages a novel Modified Wigner-Seitz Analysis to accurately quantify defect trends amidst dynamic surface reconstruction, providing a nuanced understanding of defect distribution in response to irradiation. This methodology underscores the intricate relationship between defect dynamics and the nano-scale structure of materials, specifically highlighting the role of interfaces in mediating these dynamics. The findings reveal a complex balance between defect production, surface interactions, and the influence of pre-existing defects and temperature on the primary defect production process. Surfaces are shown to amplify defect production due to biased accumulation of interstitials, alongside suppressed defect recombination, emphasizing the nuanced nature of defect dynamics in irradiated materials. This research contributes significantly to the fundamental understanding of defect formation and evolution in irradiated tungsten, offering insights that are instrumental in the development of nanomaterials poised for applications in extreme irradiation environments, such as fusion reactors, thereby advancing the field of materials science and engineering.

Keywords:

1. Introduction

Understanding the role of interfaces in defect accumulation during irradiation represents a critical step forward in the design of damage tolerant nanomaterials¹⁻³. Tailored microstructures incorporating grain and interphase boundaries provide energetically favorable sites for combating displacement damage due to irradiation¹ as well as cavity formation from gaseous impurities introduced by implantation or transmutation⁴. Interfaces have been shown to act as sinks for irradiation-induced defects where the interactions depend on the interfacial structure^{5,6}, proximity of the defects to the interface⁷, and other intrinsic factors⁸. This mechanism for limiting damage accumulation plays a significant role in nanostructured materials due to their large interfacial area per unit volume⁹, for which nanocrystalline body centered cubic (BCC) metals are of particular interest for extreme environment applications¹⁰. Tungsten presents a unique opportunity to explore nanocrystalline structures for enhanced radiation tolerance as it has emerged as the leading plasma facing material for future fusion devices¹¹⁻¹⁴ due to its attractive thermomechanical properties, resistance to sputtering, and chemical compatibility with tritium¹⁵⁻¹⁷. Indeed, various forms of nanocrystalline tungsten have demonstrated an improved radiation resistance relative to their coarse-grained counterparts¹⁸⁻²⁵. Atomistic modeling has provided critical insights into the fundamental mechanisms of defect formation and evolution during displacement cascade events in tungsten²⁶⁻²⁹ as well as the interaction of those defects with grain boundaries³⁰⁻³².

The microscopy and spectroscopy have directly identified the presence and the behaviors of the point defects³³⁻³⁵ and dislocation loops^{21,36-39} in the irradiated tungsten. Heikinheimo et al.³⁴ used the positron annihilation spectroscopy to show the mono-vacancy and self-interstitial recovery in the irradiated tungsten. In their report, the SIA migration was observed above 50K with activation energies in the range of 0.12-0.42 eV and the mono-vacancy migration was

observed above 550K with around 1.85 eV migration barrier. The defect cluster production in pure tungsten over a irradiation temperature range of 30-1073 K was summarized by Yi et al.³⁶. The TEM images well recorded the defect cluster with more than 10 atoms in size and showed that the defect production reduced with increasing temperature. These results are in line with the previous reports based on isochronal annealing tests⁴⁰⁻⁴³, which identified different recovery stages according to the resistivity curves.

By comparing the activation energy for the migration of different defects, the recovery stages of the irradiated tungsten are linked to various defect annihilation reactions⁴³⁻⁴⁶ such as free interstitial migration at stage I (below 100K), migration of shallow trapped interstitials at stage II (100K~0.15 T_m), migration of monovacancies at stage III (0.15 T_m ~0.22 T_m), dissociation of the vacancy clusters at stage IV (0.22 T_m ~0.31 T_m), and disappearance of defect clusters and formation of voids at stage V (above 0.31 T_m). Moreover, the fine structure of the recovery spectra at stage I also indicates the reactions related to several different interstitial configurations^{40,42}, possibly including dumbbell and crowdion.

Molecular dynamics (MD) simulation with well-developed interatomic potentials has reproduced many of these defect behaviors, such as the low SIA migration energy and the relatively high monovacancy migration energy^{47,48}, interstitial migration²⁸ and vacancy migration⁴⁹, various configurations of interstitials⁵⁰⁻⁵², and defect cluster formation⁵³⁻⁵⁶ and migration⁵⁷⁻⁵⁹. With the MD technique, the researchers are able to observe the structural evolution during the primary damage stage within picoseconds after the formation of the collision cascade and one of the fundamental behaviors is the focusing behavior in the crystal structure⁶⁰⁻⁶³. During the early phase of the collision cascade, the focused collision sequences (FCSs) can be produced, and those transient displacement sequences will either develop into a replacement collision on

sequences (RCSs) which link vacancies at the core and a long range interstitials, or return to the original configuration without any defect. Note that in the present study, the RCS only refers to those sequences when the atomic replacement happens, and the FCS refers any sequences caused by focusing effect.

The introduction of a free surface augments the boundary conditions along one of the simulation axes by replacing a periodic boundary with a metal-vacuum interface, which due to local relaxation, allows for a volumetric expansion in the first few lattice planes with implications for the distribution of forces on the impacting atom. This can influence defect production during impact events where the cascades interact directly with the surface and/or the thermal energy is sufficient for surviving defects to diffuse to the surface layers. Complementary atomistic simulations and experiments in Au⁶⁴, Fe^{65,66}, and W^{29,66-68} have shown that the presence of the surface altered the distribution of the primary defects prone to the surface by the formation of the stable surface defects and defect clusters. Consequently, a cascade initiated by an atom impacting a surface tends to produce more defects relative to a bulk cascade with a same damage energy. Zhong et al. ⁶⁸ compared the radial distribution functions (RDF) from the field-ion microscopy (FIM) study with the RDFs of the MD simulated surface cascade for W. The experimental results share a similar pattern with the results of the simulated surface cascade showing a significant enhancement of defect production in comparison to the bulk. In addition, cavities are detected in the irradiated thin foil tungsten, but they are absent in the bulk tungsten sample⁶⁹. The formation of the cavities is correlated to high concentration of vacancies due to the removal of the SIAs from the surfaces. Both simulation and experimental results suggest that the surface plays very important role in the radiation defect dynamics.

Internal interfaces, including grain and interface boundaries, also act as sinks for irradiation defects⁷⁰⁻⁷⁵. To estimate the behavior of the point defect near a grain boundary, Gleiter⁷³ derived a model to calculate the stress field around a grain boundary, and the stress field was shown to be a function of temperature, defect diffusivity and concentration, and characteristics of the grain boundary such as its energy and structure. This model was built to explain the behaviors during diffusional creep, however, it was also instructive to estimate the radiation defect behaviors. Based this model, Gleiter indicated that some low energy boundaries cannot act as vacancy sinks or sources (e.g. pure tilt $\Sigma 3$ GB in Cu), which was shown in radiation damage experiments^{76,77}. The recent techniques provided many other approaches to study the defect behaviors near the grain boundary, more intuitively. Uberuaga et al.⁷⁴ demonstrated in their adaptive kinetic Monte Carlo (AKMC) and accelerated molecular dynamics (AMD) calculations for Cu that the mobility of defects vary with both boundary structure and cluster size, affecting the GB sink efficiency. However, the geometry configuration, the chemical composition, and the defect state (point defect density) also affect the property of the GB^{74,75,78}. While the studies cited above focus on the proclivity for grain boundaries to accommodate radiation defects, atomistic simulations have also demonstrated that interstitial loaded grain boundaries can also act as a source for annihilation of lattice vacancies, thereby limited damage accumulation leading to void formation⁷⁸⁻⁸⁰. The related defect behaviors have also been reported in irradiated material under microscopy, such as dislocation loop absorption by the GB^{23,81}, and formation of voids at the GBs⁵.

Beyond the sink effects from free surfaces and grain boundaries, pre-existing defects from prior cascade events are also known to bias defect accumulation with insights on the fundamental mechanisms largely gained from MD simulations⁸²⁻⁸⁶. From the work of Sand et al.⁸⁶ on damage production characteristics during 50 keV cascades in Fe and W, dense pre-existing defect clusters

impacted the number of new defects created in Fe with cascade collapse occurring in the presence of pre-existing vacancy clusters. Conversely, pre-existing defects did not affect the number and distribution of defects in W, but rather augmented their morphology forming complex dislocation structures. These differences were attributed to the formation of lower energy secondary cascades in Fe promoting the formation of point defects whereas the primary cascades in tungsten led to the formation of large defect clusters⁸⁶. The experiment results also indicated the effect of the pre-existing defects on the defect production, that the defect production rate reduces, and the damage saturates as the radiation dosage increases. Thompson⁴⁶ related the dose dependent phenomenon in W to the concentration of defect sinks (vacancies, traps and grain boundaries) which can effectively remove the primary defects from the lattice, and which can also be replenished in the irradiation process. This results have been qualitatively reproduced in the MD simulation by Wu et al.⁸⁷, where the net defect production rate of the self-atom impact from the tungsten surface reduced as the damage accumulated.

Besides the structure and the pre-existing defects, the temperature also plays an role in the primary defect production process during the irradiation. Based on the irradiation damage experiments in tungsten, Yi et al.³⁷ estimated the critical dose level to reach the saturation of the loop number density, and the results showed that the critical dosage decreased with increasing temperature. A proposed explanation were formed based on the concept of the critical recombination volume^{88,89} of the defects, the interstitials and vacancies are stable if the separation distance exceeds a critical limit, while they instantly recombine for smaller separations, and the critical volume increases with higher defect mobility at the elevated temperature.

As evident in the above discussion, many of the fundamental studies on displacement cascade physics have considered defect interactions with surfaces and interfaces independently and during a single cascade event. To explore synergistic effects from a free surface and interfaces during successive cascade events where cascade overlap will influence defect accumulation, we perform MD simulations of impacting atoms on W free surfaces employing a nano-bicrystal configuration containing two different types of grain boundaries. Following the work of Frolov et al.,⁹⁰ we select two different symmetric tilt grain boundaries – $\Sigma 3\langle 110 \rangle\{112\}$ and $\Sigma 5\langle 100 \rangle\{130\}$ – which represent two low energy grain boundary configurations with different tilt axes. An impact energy of 1 keV was selected to induce the cascade within the surface layers of the nano-bicrystals, thereby promoting cascade interactions with the free surface. Our analysis focuses initially on the effect of the free surface during cascade overlap, then by reducing the effective size of the nanograin, incorporates the influence of the grain boundaries. By comparing the behavior between the two different grain boundary structures, we decouple the effects of defect formation, migration, and recombination in the context of the nature of the defects formed within the damage region and the grain boundary dependent defect segregation energies.

2. Simulation Methods

2.1 Nano-bicrystal Models

Bi-crystal models were employed to investigate the interaction of displacement cascades with grain boundaries in the presence of a free surface. Relative to typical bi-crystal models containing a single grain boundary for quantifying defect-grain boundary interactions during cascades^{31,71,78,91-95}, we required two grain boundaries to facilitate the introduction of a free surface while maintaining symmetry at the periodic boundaries normal to that surface. This configuration,

referred to as a nano-bicrystal, is illustrated in Figure 1 with the location of the external impact atom shown relative to the free surface where the dark shaded region denotes the area over which this impact was confined. Two different columnar grain sizes of 12 and 6 nm, as shown in Figure 1(a,b) respectively, were considered where the grain size was defined as the distance between the two adjacent grain boundaries. The length of the grain boundary planes along the z-direction, and thus the effective thickness of the simulation cell, was held constant at 7 nm, which was confirmed to avoid cascade interactions with the fixed bottom layer of the simulation cell. Dimensions in the x- and y-directions were also fixed at 14 and 26 nm, respectively, and the initial structures contained approximately 170,000 atoms. Two different symmetric tilt grain boundary configurations were considered for both grain size models and included a $\Sigma 3\langle 110 \rangle\{112\}$ and $\Sigma 5\langle 100 \rangle\{130\}$ grain boundary. Thus, four pristine structures were prepared for this study and denoted $\Sigma 3$ -12nm, $\Sigma 5$ -12nm, $\Sigma 3$ -6nm, and $\Sigma 5$ -6nm to capture the coincident site lattice (CSL) boundary type and effective grain size.

The nano-bicrystal models were first subjected to energy minimization and relaxation steps using molecular dynamics (MD) in the Large-scale Atomic/Molecular Massively Parallel Simulator (LAMMPS) platform⁹⁶. The bond-order interatomic potential derived by Juslin et al.⁴⁸ was employed in our simulations and has been shown to capture a realistic W-W interactions during nonequilibrium events such as collision cascades^{47,97}. To verify the accuracy of this potential for our collision cascade simulations, we calculated the threshold displacement energy along different crystallographic directions vis MD simulations and results were consistent with prior reports^{42,49,98}: 49 and 72 eV along the $\langle 100 \rangle$ and $\langle 110 \rangle$ directions, respectively. Energy minimization was conducted to achieve a final relative energy convergence of 10^{-12} with periodic boundary conditions applied in all directions. The structures were then relaxed through a simulated

annealing step by heating to 650K at a rate of 0.1 K/ps using an isothermal-isobaric ensemble where it was held for 1 ns and subsequently cooled to 300K at the same rate. Finally, following the removal of the periodic boundary along z-direction, an additional relaxation was performed for 1 ns at 300K using a Langevin thermostat to achieve a zero-pressure condition along x- and y-directions.

2.2 Collision Cascade Simulations

Displacement cascades were initiated by accelerating a tungsten atom from 2 nm above the nano-bicrystal surface from a flat emission surface randomly along the 14 nm width of the model but constrained within a 3 nm region within the center of the grains. The velocity vector of these accelerated atoms was randomly oriented within a 7° cone relative to the surface normal to suppress channeling. This constrain impact region and cone of impact are highlighted in Figure 1. To localize the cascades within proximity to the surface, the incident tungsten atom was assigned a fixed kinetic energy of 1 KeV. Consistent with prior collision cascade simulations in BCC metals^{26,54,99-101}, we neglected electronic energy losses, which are complex¹⁰²⁻¹⁰⁴ and beyond the scope of this study. Cascade evolution employed the microcanonical NVE ensemble applied for a total of 10 ps for each cascade with a time step of 0.2 fs. Atoms occupying the lower three atomic planes were fixed during the cascade simulations using freeze function to inhibit shifting of the simulation box due to energy deposition from the impacting atoms. Given the thickness of the simulation cell and kinetic energy of the impacting atoms selected to localize cascade activity near the emission surface, these fixed atomic layers did not influence evolution of the cascades. Following cascade evolution under fixed total energy and volume, the temperature of the system evolved to a temperature of approximately 325 K. At this point, the excess energy deposited in the system was

extracted through an additional 4 ps relaxation at 300 K using a Langevin thermostat. Finally, the NVE ensemble was reapplied for 2 ps prior to initiating a subsequent cascade, and this procedure was repeated for a total of 400 successive impact events.

2.3 Bulk Defect Quantification under Cascade Induced Surface Reconstruction

To produce quantitative defect trends as a function of the number of successive impacts, self-interstitial atoms and vacancies were indexed based on their occupancy of the Wigner–Seitz cells of a reference lattice. However, as shown in Figure 2a, the surface was restructured due to the impacting atoms colliding with the surface layers of the nano-bicrystal and involved adatoms from pile-up and surface accumulation concomitantly with the formation of depleted regions around the primary impact zone relative to the initial surface plane. These surface reconfigurations must be accounted for in the definition of our reference lattice as to avoid artificially inflating the number of interstitials and vacancies from the Wigner-Seitz occupancy analysis. We accomplished this by defining an extended reference lattice where the surface was “built-up” relative to the pristine structure through the addition of atoms that effectively extended the BCC lattice as shown in Figure 2b. These atoms formed a “cap” on the reference lattice relative to the pristine structure, which is used in mapping accumulated and depleted regions of the surface.

Atoms that accumulated dynamically above the original surface of the nano-bicrystal during each impact event conformed to the underlying BCC lattice. Thus, when compared with the extended reference lattice as part of the Wigner-Seitz occupancy analysis, these accumulated atoms were viewed as occupying BCC lattice sites and not quantified as interstitials in the defect analysis. Uniquely identifying these atoms, however, allowed for the number of atoms accumulated during the successive cascades to be quantified and distinguished from the total

number of implanted atoms during impact. With the number of accumulated atoms all unoccupied sites above the damaged surface were then identified through comparison with the extended reference structure to distinguish the redistribution of surface atoms during the formation of a surface crater – denoted the “depleted region” – from bulk vacancies. This process effectively created an artificial “vacancy cap” on the damaged structure, as illustrated in Figure 2c, which was composed of the free space above the damaged surface of the impacted structure (relative to the extended reference structure) and the depleted region below the original surface of the pristine structure. With the former region fully occupied in the extended reference structure, we were able to designate this region as an extended vacancy cluster in the damaged structure and remove it from the defect analysis. This left only the portion of the vacancy cap occupying the depleted region, which was excluded from the bulk vacancy analysis but used in determining the number of atoms depleted from the pristine surface during successive collisions with sputtering factored into the net depletion trends. Analysis of defects in the grain boundary regions followed an analogous treatment with the grain boundary crystallography incorporated into the extended reference structure.

3. Results and Discussion

The structure of the nano-bicrystal models and impact energy of 1 keV were deliberately selected to allow for the free surface to influence cascade evolution and thus act as a sink for point defects and mobile defect clusters. We first consider this effect by mapping defect production and the transition to vacancy saturation within the primary damage zone using the larger 12 nm grain size structure where cascades evolve independently of the grain boundaries. These trends provide insights on surface reconstruction as an energy dissipation mechanism and provide a baseline for

quantifying grain boundary effects in the presence of a free surface. Grain boundary defect production is then studied, capturing the mechanisms of grain boundary defect formation during the accumulation stages of the cascade as well as annihilation due to recombination and migration to the free surface driven by the successive cascade events. By comparing defect evolution behavior for the two different grain boundaries, we decouple mechanism-specific contributions to the cumulative grain boundary defect trends in the context of cascade driven events and diffusive processes biased by the grain boundary-dependent interstitial segregation energy.

3.1 Localized Lattice Defect Production Near a Free Surface

The cumulative number of defects during a cascade on the (110) surface of the $\Sigma 3$ -12nm structure is shown in Figure 3a during the 10 ps period where the cascade evolved under constant system energy and volume. The damage region rapidly evolves as the recoil energy is transferred via atomic collisions to the lattice with a peak damage state produced at approximately 1.2 ps. From the snapshot of the cascade at its peak damage state illustrated in the inset, recoils evolved independently of the grain boundaries, and cascade evolution in these simulations is thus akin to the bombardment of a (110) surface of a perfect BCC W lattice. Magnified snapshots of the cascade peak damage region are shown in Figure 3(b-d) at the times indicated on the cumulative defect trends where atoms fully displaced from their parent lattice sites are indexed by the larger red spheres while intermediate atomic displacements are shown as smaller spheres; all atoms displaced more than 0.5 Å are colored according to their atomic displacement. As expected in the absence of subcascade formation at the lower impact energy of 1 keV¹⁰⁵, the many recoils lead to the formation of a spatially localized displaced core^{99,106}, which is outlined using a surface mesh, and focused chain events emanating along favorable crystallographic directions well beyond this

displaced core. Athermal recombination transpired up to 4 ps with subsequent thermalization up to 10 ps, and the final state prior to relaxation is shown in Figure 3e. Here, interstitials are indexed as large red spheres, vacancies as larger blue spheres, and atoms on the BCC lattice as the smaller blue spheres; collectively, this conforms to the inset displacement scale. While the general morphological evolution of the cascade produced on the free surface was consistent with cascades produced in a perfect BCC lattice^{54,99,105-109}, all the surviving interstitials and several of the surviving vacancies were located at the surface of the nano-bicrystal.

The displaced core and recoils extending beyond its periphery inevitably interacted with the free surface as seen in the inset of Figure 3a. Since surfaces act as effective sinks for point defects¹¹⁰⁻¹¹², the number of surviving defects will be augmented relative to bulk cascades as previously reported in Fe¹¹³ and W⁶⁷. For the impact on the pristine (110) surface of the Σ 3-12nm structure shown in Figure 3, the number of surviving defects included 6 surface vacancies, 8 surface interstitials (adatoms), and 3 lattice vacancies with no interstitials remaining in the lattice. The impacting atom was effectively implanted with two atoms sputtered from the surface. For a total of 10 distinct impacts on the pristine (110) surface, the average number of defects produced were 7.0 surface vacancies, 8.7 surface interstitials (adatoms), 2.9 lattice vacancies, and <0.1 lattice interstitial. This biasing of point defects to the surface was also observed for single impacts on the (100) surface of the Σ 5-12nm, which exhibited an average of 12.1 surface vacancies, 13.2 surface interstitials, 2.5 lattice vacancies, and <0.1 lattice interstitial. The increased number of defects relative to the (110) surface impacts is attributed to the lower threshold displacement energy along the <100> direction^{42,49,98}. Inclusive of defects at the surface and within the bulk lattice, the total number of surviving defects produced by our surface impacts was 9.9 and 14.6 defects/impact for the (110) and (100) surface orientations, respectively.

The single-impact defect population produced via a 1 keV surface cascade are generally greater than the reported values for bulk cascades simulations in W with comparable PKA energies^{26,54,114,115} and the values derived from experiment results¹¹⁶⁻¹²⁰. Comparing with the database developed by Setyawan et al.⁵⁴, a 1 keV cascade in bulk tungsten produced 2.2 defects/cascade averaging over all directions. While the potential used in that study had a larger average displacement threshold energy of 128 eV, comparing defect production at identical values of the PKA energy normalized by the displacement threshold energy still did not account for the large disparity between the results obtained from our free surface simulations relative to bulk cascades. The presence of the free surface thus enhanced overall defect production with biased accumulation in the surface layers, whereas the number of interstitials surviving within the bulk was markedly reduced but with a comparable number of lattice vacancies. Similar behavior from 30 keV impacts on a tungsten surface was reported by Lee et al.⁶⁷ where a large surface concentration of interstitials was attributed to the surface sink effect and an energetic preference for the formation of adatoms. The resulting asymmetric interstitial mobility in the presence of the free surface suppressed point defect recombination, which produced many sub-surface vacancies and consistent with our results acquired under a lower PKA energy. Thus, relative to the reported trends for bulk cascades, defect production in the presence of the free surface is enhanced due to the biased accumulation of interstitials within the surface layers combined with suppressed defect recombination, which in turn reduced the number of interstitials within the bulk while having a limited impact on bulk vacancies.

3.2 Cumulative Defect Production and Vacancy Saturation

Under cumulative cascade events, the nature of the damaged surface combined with surviving lattice defects from prior cascades will ultimately influence the number of defects produced in a subsequent cascade. Shown in Figure 4a is the cumulative defect trends for the 12 nm nano-bicrystal structure containing with interstitial and vacancy trends delineated for both grain boundary types. Consistent with the biased accumulation of interstitials at the surface under a single impact, the number of interstitials remained extremely low during the first 50 impacts while the number of vacancies increased rapidly at nearly constant albeit different rates in the two structures. The moderately reduced vacancy accumulation rate in the structure containing the $\Sigma 5\langle 100 \rangle\{130\}$ grain boundaries also agreed with the single impact simulations where the average lattice vacancy rate was lower than in the $\Sigma 3\langle 110 \rangle\{112\}$ despite the larger number of total surviving defects per cascade, which is influenced by the surface sink effect as described previously. Following 50 impacts...

the accumulation of the vacancies showed a linear increase trend. In the defect accumulation results shown in Figure 4a, during the first 50 impacts, the lattice vacancies accumulated at a relatively constant rate. After 50 impacts, the consecutive impacts had a significant probability to interact with the pre-existing damage, resulting a reduction in defect production rate, or saturation of the vacancies. The defect saturation was also shown in the cumulative cascade works of Wu et al.⁸⁷ and Meyer et al.¹²¹. Wu discussed the overall defect production rate including surface defects, as the fluence went up, the overall defect production rate reduced. Since the reduction of defect production rate occurs after a critical fluence, we assume

that the cascade overlapping leads to this reduction. Gao et al.⁸³ showed that the cascade overlap in BCC iron would significantly reduce the defect production rate. For a 2 KeV cascade fully overlapped on the debris of a 2 KeV cascade, the number of surviving defects were identical to the initial number of the 2 KeV cascade debris, i.e., the consecutive cascade gained zero new defects. They noted that the pre-existing damage could shorten the RCS and assist the recombination of the Frenkel pairs within the cascade, and the damage could recombine with the defects created in the second cascade.

In the previous cascade simulation studies in the perfect lattice of other BCC metals^{26,99,106,107,122-125}, the low energy displacement cascades would generate the long-range interstitials at the cascade periphery. Stoller⁹⁹ summarized that the formation of those long-range interstitials can be a result of the replacement collision sequence (RCS) activities^{60,63,109,126,127} or shockwave-induced mechanisms^{106,108,128}. The later mechanisms relate to the high-energy cascades (above 10 KeV) and the formation of the interstitial clusters, while the RCS activities provide a way of point-defect transport from cascade core to the cascade periphery and are observed particularly at a relatively low energy. Therefore, the RCS model is more related to the interstitial formation behaviors observed in the present study. For a better understanding of the interstitial formation mechanism, a better illustration of the RCS formation is required here. The formation of the RCS is a certain type of the focusing activities^{60,61,63,129-133}. Two types of displacement sequences due to the focusing activities are presented: 1. the focused collision sequence (FCS) refers to the evolving displacement sequence; 2. the replacement collision sequence (RCS) refers to the consequence of the displacement sequence that the atoms are displaced out of their original WS cells replacing the consecutive atom at its original lattice site and forming one vacancy at one end and one interstitial at the other end. The FCS can lead to the formation of the RCS when certain

conditions are met, such as the enough initiation energy and the disrupted structure encountered by the FCS. In the perfect lattice, the collision cascade initiates the FCSs spreading along all preferential directions ($\langle 111 \rangle$ s in BCC) with a chance to form RCS, therefore, the interstitials can distribute in all directions. In the present study, the interstitials were formed mostly on the surface instead of in the lattice, resulting in the formation of adatoms. The snapshots shown in Figure 3b-e showed significant number of FCSs were formed at the peak of the cascade, spreading from the PDR, forming some temporary displacement chains, and returning within 1ps. However, the RCS was absent from the scene. The suppressing of the RCS formation then resulted in a reduced production rate of lattice interstitials. For the 1 KeV bombardment on (100) and (110) surfaces, the lattice interstitial production rates were both extremely low as 0.04 per impact comparing the lattice vacancy production rates of 2.5 and 3.0 per impact respectively. These vacancy production rates quite fit the number given for the case in the bulk tungsten: ~ 2 surviving Frenkel pairs per 1 KeV cascade as discussed above^{26,54,114-120}.

After the defects were created, the consecutive bombardment continued, and the defect distribution kept evolving until the final dose. Under the simulation condition, the most vibrant defects were interstitials. It was known that the mobility of the interstitial in BCC metals depends significantly on the interstitial configuration^{28,50}. By investigation of the atomic structure near interstitials in the final state (Figure 5a), the interstitials can be in a couple of configurations, (1) the dumbbell configuration (Figure 5b) and (2) the crowdion configuration (Figure 5c) as well as (3) interstitial cluster (Figure 5d). Beside those configurations, the crowdion was reported to have a migration temperature as low as 30K¹³⁴⁻¹³⁶ and a migration energy as low as 2.6 meV^{28,135,136} or 0.05 eV¹³⁷, while the migration temperature for the vacancy was reported to be around 700K^{138,139} and the migration energy was reported to be 1.78eV^{28,140}. The SIA migration dominated the

thermal defect annealing process up to 2050K¹⁴¹. Under the present simulation condition at 300K, the crowdion was able to migrate spontaneously in the lattice. Because of the high mobility during the simulation, interstitials were observed to join and form interstitial clusters occasionally within nanosecond scale. As a comparison, no vacancy cluster was observed to form in the lattice, due to lack of mobility as well as unfavorable process of two mono vacancies forming one di-vacancy^{140,142}.

As indicated in the previous chapter, the overlap of the collision cascades resulted in effectively reduced new defect production. Therefore, after the critical fluence, when the overlap probability was close to 100%, the defects in the structure would reach their saturation point, such as the lattice vacancy shown in Figure 4a. Based on the previous study⁸³ and our observations, the consecutive cascade in the pre-damaged area only heated the area without transporting interstitials out of the spot. For a 1 KeV cascade, the Frenkel pair recombination zone was large enough to enclose the PDR, therefore, in the vacancy-rich PDR, the interstitials could not survive at a discernible probability. Without interstitial transport, the consecutive cascade was not able to significantly affect the defect concentration in the pre-existing PDR.

However, the detailed mechanism of suppressing the interstitial transport was not clear, presumably due to the absence of the RCS formation mechanism caused by the excess vacancies in the region. Byggmästar et al.⁸⁴ and Granberg et al.¹⁴³ studied the cascade overlapping effects in BCC metals with the pre-existing interstitial type of defects and the vacancy type of defects in the cascade core. Both types of defects reduced the new defect production rate, and the production

rate reduction was more drastic when the cascade overlapped the interstitial type defect. The similarity between two types of defects was that they both distorted the lattice structure. As a type of focusing activity^{129,144}, the RCS formation was sensitive to the lattice alignment. The lattice structure misalignment by the defects contributed the suppressing of the RCS formation, and resulted in the reduction of the defect production.

Based on the cascade overlap induced defect production reduction, a prediction of the surviving number of defects in the structure was established with the overlap probability and the base defect production rate. Assuming that the size of PDR was consistent throughout the simulation, the overlap probability of nth impact falling into the previous PDRs can be calculated as:

$$\text{Equation 1} \quad P_{overlap}^n = 1 - P_{miss} = 1 - \left(1 - \frac{S_{PDR}}{S_{area}}\right)^{n-1}$$

where S_{PDR} is the area of the PDR, and the S_{area} is the area of the bombardment area. In our simulation, S_{PDR} is around 2nm^2 (0.8nm in radius), and S_{area} is 52nm^2 . Since the PDR is small in size, a binary approximation is applied here: (a) the consecutive PDR in the pre-existing PDR produces zero net defects, and (b) the PDR out of the pre-existing PDR produces a consistent number of defects (N_{each}), the number of surviving defects after nth impact can be modeled by:

$$\begin{aligned} \text{Equation 2} \quad N_n &= \sum_1^n (P_{miss} \times N_{each}) = \sum_1^n \left(\left(1 - \frac{S_{PDR}}{S_{area}}\right)^{n-1} \times N_{each} \right) \\ N_n &= N_{each} \times \frac{1 - (1 - a)^n}{a}, a = \frac{S_{PDR}}{S_{area}} \end{aligned}$$

For example, in Figure 6a, the number of lattice vacancies in $\Sigma 3$ -12nm structure with {110} surface was estimated based on Equation 2, $N_{each} = 3$ (for $\Sigma 5$ -12nm structure with {100} surface, $N_{each} = 2.5$), the results from the simulation oscillated around the predicted line. The accumulation of all defect types that had a chance to survive after the recombination phase were affected by the

cascade overlap effect in a similar manner. In contrast, other events happened during the ballistic evolution kept the production rate consistent throughout the simulation, such as sputtering (rate of 2.0 per impact), and implantation (rate of 1.0 per impact).

The surface accumulation and the surface depletion showing in the upper part of Figure 6b indicated that the surface valley and the surface hill built up at a higher rate before the PDR saturation point. After the saturation point, the surface valley deepened at a similar rate as the sputtering rate, and the surface hill grew at a similar rate as implantation rate. For a better understanding of the overlap effect on the mass transfer excluding implantation and sputtering, the overlap effects on the surface accumulation and surface depletion were re-illustrated by the net accumulation and the net depletion, as Figure 6b. Net accumulation represented the atoms accumulated onto the surface hill excluding implantation, and net depletion counted the atoms displaced from the surface valley excluding the sputtering:

$$\text{Equation 3} \quad \textit{Net Accumulation} = \textit{Surface Accumulation} - \textit{Implanted Atoms}$$

$$\text{Equation 4} \quad \textit{Net Depletion} = \textit{Surface Depletion} - \textit{Sputtered Atoms}$$

As shown in Figure 6b, the net accumulation and net depletion also saturated when overlap probability was close to 1. The trends suggested that the mass transfer between the surface valley and the surface hill came to a balance after the saturation point. The saturated number of the net accumulation was higher than that of the net depletion, and the difference equaled the production difference of lattice vacancies and lattice interstitials, the atoms from the excess lattice vacancy sites were accumulated onto the surface.

3.3 Biased Defect Production in Grain Boundaries

When the GBs were fabricated closer to the bombardment area as in $\Sigma 3$ -6nm and $\Sigma 5$ -6nm structures, the GB was not in reach of the PDR but was able to interact with the FCs of the cascade. Based on the Pérez-Pérez and Smith⁹⁴ modeling work on the cascade evolution in the vicinity of the bcc iron GB, the GB would collect some interstitials through the RCSs from the cascade. In the present cumulative bombardment simulation in $\Sigma 3$ -6nm and $\Sigma 5$ -6nm structures, the GB interstitial accumulation was also observed as in Figure 7b-c. Although more interstitials were formed below the surface, the lattice vacancies in $\Sigma 3$ -6nm and $\Sigma 5$ -6nm structures showed similar trend as in the structures with 12nm center grain. Therefore, the discussion of the biased defect accumulation near GBs will focus on the behaviors of the interstitials.

It was reported that the accumulation of the interstitials in the GB plane would change the GB structure^{93,95}, to systematically calculate the defect distribution in those deformed structures, the modified WS analysis was applied. The excessive interstitial production in Figure 7a was revealed in Figure 8 that although a considerable number of interstitials were collected by the GBs, the trends of the lattice defects in the 6nm structure was identical to that in the 12nm structure. The damage accumulated in the GB contributed the most interstitial production under the surface. Besides, the GB structure also affected the GB interstitial behaviors, as was reported by Esfandiarpour et al.⁹² and Zhang et al.³¹. In the present study, the $\Sigma 5$ GB collected more interstitials after 400 cumulative impacts than the $\Sigma 3$ GB. For the defect production mechanisms, we generally accepted the shockwave model of the collision cascade evolution as Calder et al. detailly described in Ref.¹⁰⁸, and the cascade-defect interactions summarized by Wang et al. in Ref.¹⁴⁵. The shockwave model provided the defect production within the cascade ballistic phase, and the

cascade-defect interactions guided the search for behaviors beyond the ballistic phase. The detailed mechanisms will be discussed in the later sections.

3.4 Grain Boundary Defect Evolution During Successive Cascades

Searching through all GB interstitial creation events, we identified two general GB interstitial production mechanisms in the present simulations: (1) the formation of RCS from the GB's trapping of the FC during the ballistic phase, and (2) thermal interstitial migration after the recombination phase.

The first approach was showed in Figure 9. The CC-GB interaction related GB defect production was observed in both $\Sigma 3$ and $\Sigma 5$ GB configurations. In the present work, the snapshots indicated that the presence of the GB can trap the FCs and form RCSs, when the RCSs were formed the interstitials were transferred from the cascade core to the GB as the atomic displacements shown in Figure 9b and d. Based on the shockwave model, when the shockwave front, which had a higher atomic density, reached an obstacle, the progress would stop. Then, the trailing part would squeeze the leading part, forming the RCSs. Those RCSs would result in the interstitials near the obstacle and vacancies near the cascade core. In the present simulations, due to the low energy settings, the shockwaves were in the form of the focusing chains. The transmission of those FCs would be obstructed by the GB. When obstructed, the RCSs would form between the PDR and the GB, creating interstitials at GB and vacancies in the PDR. Then, the interstitial segregation energy (binding energy) at GB would trap the interstitials preventing the interstitial emission without other excitations. This GB interstitial production process was observed in both GBs almost at a similar occurrence rate.

To better illustrate this process, controlled simulations were conducted in order to verify the detailed mechanisms, as shown in Figure 10a-b. An atom 2 nm away from the $\Sigma 5$ GB was accelerated along $\langle 111 \rangle$ direction towards the GB at initial energy levels from 1 to 70 eV. The calculation showed that the threshold displacement energy (TDE) to create an interstitial dropped from 64eV in perfect lattice to 55eV in the presence of the $\Sigma 5$ GB. However, the controlled simulation showed a different FC trapping behavior from the bombardment simulation. When the GB trapped the focusing chain in the controlled simulation, the vacancy was created adjacent to the GB, while in the cascade simulation, the vacancies were created in the PDR. This indicated that the cascade may also affect this FC trapping behavior, presumably by pressing the trailing part of the FC or by energizing the lattice for an even lower TDE.

When the GB interstitials were formed, the configurations were affected by the GB structure, as shown in Figure 10c-d. The configuration affected the strength of the interaction between the interstitial and the GB. The interstitial in $\Sigma 3$ GB was in a mobile configuration, while the interstitial in $\Sigma 5$ GB stayed in a stable pentagonal cage. The difference implied the varying trapping strength on GB interstitial and the varying rate of the GB interstitial emission.

The second approach for GB interstitial formation was shown in Figure 11. Two GB configurations demonstrated different attraction behavior of the nearby interstitials. Figure 11a-b showed a crowdion cluster near a $\Sigma 5$ GB migrated into the GB along $\langle 111 \rangle$ direction. In contrast of Figure 11c-d, instead of migrating into the GB, a $\langle 111 \rangle$ crowdion near a $\Sigma 3$ GB at a similar distance rotated to the less mobile $\langle 110 \rangle$ dumbbell configuration. The reason for this transformation may be that although the dumbbell configuration had a slightly higher energy than the crowdion configuration, $\sim 0.25\text{eV}$ as reported in Ref. ^{52,137,146}, the energy difference was not significant enough to prevent the transformation at 300K. As in the works of Ma et al. ⁵² and

Ventelon et al.¹⁴⁶, they predicted a symmetry-broken self-interstitial configuration in tungsten, denoted as $\langle 11\xi \rangle$ dumbbell, which shared some decisive features with the $\langle 111 \rangle$ crowdion configuration observed in the present study as shown in Figure 5c. The migration of the $\langle 11\xi \rangle$ dumbbell started with transforming to the $\langle 111 \rangle$ crowdion, therefore, the lattice structure near the GB (shown in **Error! Reference source not found.**) may also affect the interstitial migration behavior.

This migration-related GB interstitial formation process happened significantly more frequently at $\Sigma 5$ GBs than at $\Sigma 3$ GBs. Besides the structural differences between these two GBs, the different interstitial segregation energy in the vicinity of the GB may also play a role. Here, the interstitial segregation energy was defined as the energy change when the lattice interstitial moved into the GB. As in Ref.⁷⁴, Uberuaga et al. demonstrated that the flux of the defects to the GB relative to the flux of the defects to the ideal sink, which was defined as the sink efficiency, would be affected by the defect migration barrier and the defect binding energy at the GB (similar to the segregation energy in the present study). A GB with higher sink efficiency would behave more like a perfect defect sink that would efficiently remove the defects from the lattice given enough time for evolution. Although the present study didn't last long enough to reveal the final defect state, the sink efficiency of the GB was supposed to affect the defect accumulation rate during a same period of time.

Besides the GB interstitial production processes, the number of GB interstitials can also be affected by GB interstitial elimination processes. Two GB interstitial elimination processes observed in the present study were both related to the GB interstitial emission after excitation. As shown in Figure 12, when excited by the nearby cascade, the GB interstitials would jump out of the GB. If a vacancy was presented nearby, the interstitial would recombine with the vacancy

(Figure 12a-d). If the GB interstitial was close to the surface, it would migrate to the surface (Figure 12e-h). The interstitials were immobile at the background temperature of 300K. At the beginning of two events Figure 12a and e, the GB interstitials were initially in the dumbbell form. When the shockwave reached the GB, the interstitial turned into the crowdion form with higher mobility. Those crowdions then migrated to the configurations with lower energy.

Although these interstitial migrations under excited state haven't been well studied to our best knowledge, the work by Bai et al.⁷⁸ provided some insights on the general factors that would affect the defect behaviors in the vicinity of the GB. In Ref.⁷⁸, Bai et al. reported that when the vacancies were presented in the vicinity of the GB interstitial along the preferential migration direction, the interstitial emission would happen through a replacement process with a much smaller energy barriers. However, considering the occurrence rate difference, the presence of the nearby vacancies cannot be the only factor for the interstitial emission observed in the present study. The observations indicated that both the nearby interstitial sink (the surface and the vacancy) and the energy to activate the GB interstitial accelerated the emission of the GB interstitials. Intuitively, these process should be affected by the GB configuration, therefore, two GBs tested in the present study would show different GB interstitial emission effects.

3.5 Mechanistic Contributions and Defect Segregation Energy Landscapes

To summarize the previous section and systemically compare the GB effects on GB defect evolution during the simulation, different mechanistic contributions to the GB interstitial evolution were plotted in Figure 13a for $\Sigma 3$ -6nm structure and Figure 13b for $\Sigma 5$ -6nm structure. The mechanisms included (1) the RCS formation by GB trapping of FC, (2) the interstitial thermal migration to the GB, (3) the GB interstitial migration to surface, and (4) the GB interstitial

recombination with the adjacent vacancy. The contributions of GB interstitials from the RCS formation were similar between two structures since both GBs would be the effective obstacles for the FCs. Whereas the contributions from the two GB interstitial emission mechanisms were significantly different between two structures, probably due to configuration and the sink efficiency differences. Configurationally, the interstitials in the $\Sigma 5$ GB were less likely to be energetically activated than in the $\Sigma 3$ GB configuration, as the latter was a mobile crowdion-like configuration and the former was in a stable form. Figure 13b showed a higher interstitial migration contribution to the accumulation of the GB interstitials in the $\Sigma 5$ GB compared to that in the $\Sigma 3$ GB, and the interstitials in the $\Sigma 5$ GB didn't migrate out of the GB until the GB was highly loaded with interstitials.

Based on the sink efficiency explanations ⁷⁴, the differences in the contributions of interstitial thermal migration to the GB and the interstitial emission behaviors can be well explained by the interstitial segregation energy landscapes in the vicinity of the GBs, shown in **Error! Reference source not found.** The depths of energy barrier in two different GB configurations were significantly different. In $\Sigma 5$ GB, the barrier was more than twice as high as in the $\Sigma 3$ GB (i.e., 6.5eV and 3eV, respectively). The segregation energy landscape near the $\Sigma 5$ GB had a steeper and deeper shape than that near the $\Sigma 3$ GB, indicating that the $\Sigma 5$ GB would have a higher sink efficiency than the $\Sigma 3$ GB. The $\Sigma 5$ GB with higher sink efficiency would behave more like a perfect interstitial sink being able to collect the nearby interstitials with a higher efficiency, and that once the interstitial fell into the GB, it would be less likely for it jump out of the $\Sigma 5$ GB under the same conditions as the $\Sigma 3$ GB. Therefore, the thermal migration contribution to the number of GB interstitials was higher in the $\Sigma 5$ -6nm structure (Figure 13a) than in the $\Sigma 3$ -6nm

structure (Figure 13b) and the GB interstitial annihilation processes occurred at a higher rate in the $\Sigma 5$ -6nm structure (Figure 13a) than in the $\Sigma 3$ -6nm structure (Figure 13b).

4. Conclusions

Molecular dynamics simulations of self-ion irradiation on Tungsten with surface demonstrated that two significant sources of the point defects were actively involved in the defect production and distribution process. A useful Modified WS Analysis method was developed to reveal the details of such behaviors in a complicated and dynamically changing structure. The narrowing of the center grain size activated new mechanisms of defect production with the majority happened inside the GBs. The manifestation of these processes in the categorized defect evolution trends combined with controlled comparisons provided new insights into the dependence of GB configuration, overlap probability, interstitial configuration, and interstitial segregation energy as follows:

- i. For the irradiation on the surface without GB interaction: the production rate of the defects created in PDR depended on thermodynamic defect formation energy, due to the limited long-range defect production rate and enhanced in-cascade recombination.
- ii. Since the surviving defects in PDR were created through a thermodynamic approach, the successive impacts on the pre-damaged area significantly reduced the new defect production rate on average. After the critical fluence, the numbers of defects in PDR saturated as the overlap probability close to 100%. The equation of the overlap probability (**Error! Reference source not found.**) followed the accumulation of the surviving defects in the PDR.

- iii. The dynamic crowdion migration would promote the creation of more interstitials in the structure. However, due to the thermodynamic approach in the “quasi-liquid” core, the number of lattice vacancies didn’t show an increase. The type of GB didn’t affect the rate of the GB interstitial production by dynamic crowdion.
- iv. The thermal migration of interstitials from the lattice into the grain boundary, as another way of GB interstitial creation, was possibly driven by the sink efficiency of the GB, which was suggested to be segregation energy (binding energy) dependent.
- v. The GB interstitials could also jump out of the GB and relocate to lower energy configuration if the interstitials were enclosed in the collision cascade.

These results showed significantly different defect production behaviors in the collision cascade near the surface compared with the process in the bulk material. This would contribute to the estimation of the surface property change during the low energy irradiation. The presence of the GB near the surface region enhanced the interstitial formation in the structure, while the GB didn’t exhibit a discernible effect on vacancy production. This would suggest an enhancement of radiation tolerance, since the GB interstitials may also jump out from the GB and recombine with the adjacent vacancies. The interstitials showed a higher emission fraction (emission/loaded) from GB with lower binding energy, suggesting that the GB with lower binding energy may provide more improvement. Further investigations are needed to develop a deeper understanding of the enhancement.

Acknowledgements

This work was supported by the U.S. Department of Energy, Office of Fusion Energy Sciences, under contract DE-SC0017899.

References

- 1 I. J. Beyerlein, A. Caro, M. J. Demkowicz, N. A. Mara, A. Misra, and B. P. Uberuaga, *Materials Today* **16**, 443 (2013).
- 2 S. Wurster and R. Pippin, *Scripta Materialia* **60**, 1083 (2009).
- 3 G. Ackland, *Science* **327**, 1587 (2010).
- 4 H. Trinkaus and B. N. Singh, *Journal of Nuclear Materials* **323**, 229 (2003).
- 5 W. Z. Han, M. J. Demkowicz, E. G. Fu, Y. Q. Wang, and A. Misra, *Acta Materialia* **60**, 6341 (2012).
- 6 X. M. Bai, L. J. Vernon, R. G. Hoagland, A. F. Voter, M. Nastasi, and B. P. Uberuaga, *Physical Review B* **85** (2012).
- 7 A. Misra, M. J. Demkowicz, X. Zhang, and R. G. Hoagland, *Jom* **59**, 62 (2007).
- 8 I. J. Beyerlein, M. J. Demkowicz, A. Misra, and B. P. Uberuaga, *Progress in Materials Science* **74**, 125 (2015).
- 9 M. J. Demkowicz, R. G. Hoagland, B. P. Uberuaga, and A. Misra, *Physical Review B* **84** (2011).
- 10 B. E. Schuster, J. P. Ligda, Z. L. Pan, and Q. Wei, *Jom* **63**, 27 (2011).
- 11 V. Philipps, *Journal of Nuclear Materials* **415**, S2 (2011).
- 12 Y. Huang, M. S. Tillack, and N. M. Ghoniem, *Fusion Engineering and Design* **135**, 346 (2018).
- 13 R. Neu, R. Dux, A. Kallenbach, T. Putterich, M. Balden, J. C. Fuchs, A. Herrmann, C. F. Maggi, M. O'Mullane, R. Pugno, I. Radivojevic, V. Rohde, A. C. C. Sips, W. Suttrop, A. Whiteford, and A. U. team, *Nuclear Fusion* **45**, 209 (2005).
- 14 R. A. Pitts, S. Carpentier, F. Escourbiac, T. Hirai, V. Komarov, S. Lisgo, A. S. Kukushkin, A. Loarte, M. Merola, A. S. Naik, R. Mitteau, M. Sugihara, B. Bazylev, and P. C. Stangeby, *Journal of Nuclear Materials* **438**, S48 (2013).
- 15 S. J. Zinkle and L. L. Snead, *Annual Review of Materials Research* **44**, 241 (2014).
- 16 Y. Ueda, J. W. Coenen, G. De Temmerman, R. P. Doerner, J. Linke, V. Philipps, and E. Tsitrone, *Fusion Engineering and Design* **89**, 901 (2014).
- 17 S. Wurster, N. Baluc, M. Battabyal, T. Crosby, J. Du, C. García-Rosales, A. Hasegawa, A. Hoffmann, A. Kimura, H. Kurishita, R. J. Kurtz, H. Li, S. Noh, J. Reiser, J. Riesch, M. Rieth, W. Setyawan, M. Walter, J. H. You, and R. Pippin, *Journal of Nuclear Materials* **442**, S181 (2013).
- 18 H. Kurishita, S. Kobayashi, K. Nakai, T. Ogawa, A. Hasegawa, K. Abe, H. Arakawa, S. Matsuo, T. Takida, K. Takebe, M. Kawai, and N. Yoshida, *Journal of Nuclear Materials* **377**, 34 (2008).
- 19 O. El-Atwani, W. S. Cunningham, E. Esquivel, M. Li, J. R. Trelewicz, B. P. Uberuaga, and S. A. Maloy, *Acta Materialia* **164**, 547 (2019).
- 20 O. El-Atwani, N. Li, M. Li, A. Devaraj, J. K. S. Baldwin, M. M. Schneider, D. Sobieraj, J. S. Wróbel, D. Nguyen-Manh, S. A. Maloy, and E. Martinez, *Science Advances* **5**, eaav2002 (2019).
- 21 O. El-Atwani, E. Esquivel, M. Efe, E. Aydogan, Y. Q. Wang, E. Martinez, and S. A. Maloy, *Acta Materialia* **149**, 206 (2018).
- 22 O. El-Atwani, E. Esquivel, E. Aydogan, E. Martinez, J. K. Baldwin, M. Li, B. P. Uberuaga, and S. A. Maloy, *Acta Materialia* **165**, 118 (2019).
- 23 W. S. Cunningham, K. Hattar, Y. Zhu, D. J. Edwards, and J. R. Trelewicz, *Acta Materialia* **206**, 116629 (2021).

24 H. W. Wang, Y. Gao, E. G. Fu, T. F. Yang, S. Yan, J. M. Xue, P. K. Chu, and Y. G. Wang,
Journal of Nuclear Materials **442**, 189 (2013).

25 H. Xu, L.-L. He, Y.-F. Pei, C.-Z. Jiang, W.-Q. Li, and X.-H. Xiao, Tungsten **3**, 20 (2021).

26 W. Setyawan, G. Nandipati, K. J. Roche, H. L. Heinisch, B. D. Wirth, and R. J. Kurtz,
Journal of Nuclear Materials **462**, 329 (2015).

27 S. Wahyu, P. S. Aaron, J. Niklas, E. S. Roger, D. W. Brian, and J. K. Richard, Journal of
Physics: Condensed Matter **27**, 225402 (2015).

28 T. D. Swinburne, P.-W. Ma, and S. L. Dudarev, New Journal of Physics **19**, 073024 (2017).

29 Y. Wu, P. Krstic, F. Y. Zhou, and F. Meyer, Journal of Nuclear Materials **467**, 480 (2015).

30 X.-Y. Li, Y.-G. Zhang, Y.-C. Xu, X.-B. Wu, X.-S. Kong, X.-P. Wang, Q.-F. Fang, and C.-
S. Liu, Tungsten (2020).

31 C. G. Zhang, W. H. Zhou, Y. G. Li, Z. Zeng, and X. Ju, Journal of Nuclear Materials **458**,
138 (2015).

32 M. R. Gilbert, K. Arakawa, Z. Bergstrom, M. J. Caturla, S. L. Dudarev, F. Gao, A. M.
Goryaeva, S. Y. Hu, X. Hu, R. J. Kurtz, A. Litnovsky, J. Marian, M. C. Marinica, E.
Martinez, E. A. Marquis, D. R. Mason, B. N. Nguyen, P. Olsson, Y. Osetskiy, D. Senor,
W. Setyawan, M. P. Short, T. Suzudo, J. R. Trelewicz, T. Tsuru, G. S. Was, B. D. Wirth,
L. Yang, Y. Zhang, and S. J. Zinkle, Journal of Nuclear Materials **554**, 153113 (2021).

33 M. Attardo and J. M. Galligan, *physica status solidi (b)* **16**, 449 (1966).

34 J. Heikinheimo, K. Mizohata, J. Räisänen, T. Ahlgren, P. Jalkanen, A. Lahtinen, N.
Catarino, E. Alves, and F. Tuomisto, APL Materials **7**, 021103 (2019).

35 D. Seidman, Journal of Physics F: Metal Physics **3**, 393 (1973).

36 X. Yi, M. L. Jenkins, M. A. Kirk, Z. Zhou, and S. G. Roberts, Acta Materialia **112**, 105
(2016).

37 X. Yi, M. L. Jenkins, K. Hattar, P. D. Edmondson, and S. G. Roberts, Acta Materialia **92**,
163 (2015).

38 X. Yi, M. L. Jenkins, M. Briceno, S. G. Roberts, Z. Zhou, and M. A. Kirk, Philosophical
Magazine **93**, 1715 (2013).

39 D. R. Mason, X. Yi, M. A. Kirk, and S. L. Dudarev, J Phys Condens Matter **26**, 375701
(2014).

40 H. H. Neely, D. W. Keefer, and A. Sosin, Physica Status Solidi (b) **28**, 675 (1968).

41 L. Keys, J. Smith, and J. Moteff, Physical Review **176**, 851 (1968).

42 F. Maury, M. Biget, P. Vajda, A. Lucasson, and P. Lucasson, Radiation Effects **38**, 53
(1978).

43 L. Keys and J. Moteff, Journal of Nuclear Materials **34**, 260 (1970).

44 F. Ferroni, X. Yi, K. Arakawa, S. P. Fitzgerald, P. D. Edmondson, and S. G. Roberts, Acta
Materialia **90**, 380 (2015).

45 V. N. Bykov, G. A. Birzhevoi, M. I. Zakharova, and V. A. Solov'Ev, Soviet Atomic Energy
33, 930 (1972).

46 M. Thompson, Philosophical Magazine **5**, 278 (1960).

47 T. Ahlgren, K. Heinola, N. Juslin, and A. Kuronen, Journal of Applied Physics **107**, 033516
(2010).

48 N. Juslin, P. Erhart, P. Träskelin, J. Nord, K. O. E. Henriksson, K. Nordlund, E. Salonen,
and K. Albe, Journal of Applied Physics **98**, 123520 (2005).

49 Q. Xu, T. Yoshiie, and H. C. Huang, Nuclear Instruments and Methods in Physics Research
Section B: Beam Interactions with Materials and Atoms **206**, 123 (2003).

50 P. M. Derlet, D. Nguyen-Manh, and S. L. Dudarev, *Physical Review B* **76**, 054107 (2007).
51 L. Chen, Y. Liu, H. Zhou, S. Jin, Y. Zhang, and G. Lu, *Science China Physics, Mechanics
and Astronomy* **55**, 614 (2012).
52 P.-W. Ma and S. L. Dudarev, *Physical Review Materials* **3** (2019).
53 A. E. Sand, M. J. Aliaga, M. J. Caturla, and K. Nordlund, *EPL (Europhysics Letters)* **115**
(2016).
54 W. Setyawan, A. P. Selby, N. Juslin, R. E. Stoller, B. D. Wirth, and R. J. Kurtz, *Journal of
Physics: Condensed Matter* **27**, 225402 (2015).
55 A. E. Sand, S. Dudarev, and K. Nordlund, *EPL (Europhysics Letters)* **103**, 46003 (2013).
56 Q. Peng, F. Meng, Y. Yang, C. Lu, H. Deng, L. Wang, S. De, and F. Gao, *Nat Commun* **9**,
4880 (2018).
57 B. Wirth, G. Odette, D. Maroudas, and G. Lucas, *Journal of nuclear materials* **244**, 185
(1997).
58 N. Soneda and T. Diaz de La Rubia, *Philosophical Magazine A* **81**, 331 (2001).
59 W. Zhou, C. Zhang, Y. Li, and Z. Zeng, *Journal of Nuclear Materials* **453**, 202 (2014).
60 C. S. Becquart, A. Souidi, and M. Hou, *Philosophical Magazine* **85**, 409 (2006).
61 A. Foreman, C. English, and W. Phythian, *Philosophical Magazine A* **66**, 655 (1992).
62 K. Nordlund, S. J. Zinkle, A. E. Sand, F. Granberg, R. S. Averback, R. Stoller, T. Suzudo,
L. Malerba, F. Banhart, and W. J. Weber, *Nature communications* **9**, 1 (2018).
63 M. Hou, A. Souidi, and C. S. Becquart, *Nuclear Instruments and Methods in Physics
Research B* **196**, 8 (2002).
64 M. Ghaly and R. S. Averback, *Physical Review Letters* **72**, 364 (1994).
65 R. E. Stoller, *Journal of nuclear materials* **307**, 935 (2002).
66 A. E. Sand, M. Aliaga, M. J. Caturla, and K. Nordlund, *EPL (Europhysics Letters)* **115**,
36001 (2016).
67 H. G. Lee, S. Yoo, B. Lee, and K. Kang, *Nuclear Fusion* **60**, 126009 (2020).
68 Y. Zhong, K. Nordlund, M. Ghaly, and R. S. Averback, *Physical Review B* **58**, 2361 (1998).
69 R.-Y. Zheng and W.-Z. Han, *Acta Materialia* **186**, 162 (2020).
70 M. Ashby, *Scripta Metallurgica* **3**, 837 (1969).
71 X. Li, W. Liu, Y. Xu, C. Liu, Q. Fang, B. Pan, J.-L. Chen, G.-N. Luo, and Z. Wang, *Nuclear
Fusion* **53**, 123014 (2013).
72 O. El-Atwani, J. E. Nathaniel, A. C. Leff, K. Hattar, and M. L. Taheri, *Sci Rep* **7**, 1836
(2017).
73 H. Gleiter, *Acta Metallurgica* **27**, 187 (1979).
74 B. P. Uberuaga, L. J. Vernon, E. Martinez, and A. F. Voter, *Sci Rep* **5**, 9095 (2015).
75 M. A. Tschopp, K. N. Solanki, F. Gao, X. Sun, M. A. Khaleel, and M. F. Horstemeyer,
Physical Review B **85** (2012).
76 R. Barnes, G. Redding, and A. Cottrell, *Philosophical Magazine* **3**, 97 (1958).
77 R. Barnes, *Philosophical Magazine* **5**, 635 (1960).
78 X.-M. Bai, A. F. Voter, R. G. Hoagland, M. Nastasi, and B. P. Uberuaga, *Science* **327**,
1631 (2010).
79 X. Li, Y. Xu, G. Duan, J. Sun, C. Hao, Y. Zhang, W. Liu, C. Liu, and Q. Fang, *Journal of
Nuclear Materials* **500**, 199 (2018).
80 X. Li, G. Duan, Y. Xu, Y. Zhang, W. Liu, C. S. Liu, Y. Liang, J.-L. Chen, and G.-N. Luo,
Nuclear Fusion **57**, 116055 (2017).

81 O. El-Atwani, A. Suslova, T. J. Novakowski, K. Hattar, M. Efe, S. S. Harilal, and A.
Hassanein, *Materials Characterization* **99**, 68 (2015).
82 C. English, W. Phythian, and A. Foreman, *Journal of nuclear materials* **174**, 135 (1990).
83 F. Gao, D. Bacon, A. Calder, P. Flewitt, and T. Lewis, *Journal of nuclear materials* **230**, 47
(1996).
84 J. Byggmästar, F. Granberg, A. E. Sand, A. Pirttikoski, R. Alexander, M.-C. Marinica, and
K. Nordlund, *Journal of Physics: Condensed Matter* **31**, 245402 (2019).
85 A. Fellman, A. E. Sand, J. Byggmastar, and K. Nordlund, *J Phys Condens Matter* **31**,
405402 (2019).
86 A. E. Sand, J. Byggmästar, A. Zitting, and K. Nordlund, *Journal of Nuclear Materials* **511**,
64 (2018).
87 Y. Wu, P. Krstic, F. Y. Zhou, and F. Meyer, *Journal of Nuclear Materials* **467**, 480 (2015).
88 G. Kinchin and R. Pease, *Reports on progress in physics* **18**, 1 (1955).
89 J. Horak and T. Blewitt, *physica status solidi (a)* **9**, 721 (1972).
90 T. Frolov, Q. Zhu, T. Ooppelstrup, J. Marian, and R. E. Rudd, *Acta Materialia* **159**, 123
(2018).
91 C. P. Xu, X. Y. Liu, F. Gao, Y. H. Li, and Y. Q. Wang, *Nuclear Instruments and Methods
in Physics Research Section B: Beam Interactions with Materials and Atoms* **332**, 426
(2014).
92 A. Esfandiarpour, S. A. H. Fegghi, and A. A. Shokri, *Nuclear Instruments and Methods in
Physics Research Section B: Beam Interactions with Materials and Atoms* **362**, 1 (2015).
93 F. J. Perez-Perez and R. Smith, *Nuclear Instruments and Methods in Physics Research
Section B: Beam Interactions with Materials and Atoms* (2000).
94 F. J. Perez-Perez and R. Smith, *Nuclear Instruments and Methods in Physics Research
Section B: Beam Interactions with Materials and Atoms* (1999).
95 F. J. Perez-Perez and R. Smith, *Nuclear Instruments and Methods in Physics Research
Section B: Beam Interactions with Materials and Atoms* **180** (2001).
96 S. Plimpton, *Journal of computational physics* **117**, 1 (1995).
97 N. Juslin, V. Jansson, and K. Nordlund, *Philosophical Magazine* **90**, 3581 (2010).
98 M. J. Banisalman, S. Park, and T. Oda, *Journal of Nuclear Materials* **495**, 277 (2017).
99 R. Stoller, *Comprehensive nuclear materials*, 293 (2012).
100 R. Stoller, G. Odette, and B. Wirth, *Journal of Nuclear Materials* **251**, 49 (1997).
101 A. P. Selby, D. Xu, N. Juslin, N. A. Capps, and B. D. Wirth, *Journal of Nuclear Materials*
437, 19 (2013).
102 A. Caro and M. Victoria, *Physical Review A* **40**, 2287 (1989).
103 C. Race, D. Mason, M. Finnis, W. Foulkes, A. Horsfield, and A. Sutton, *Reports on
Progress in Physics* **73**, 116501 (2010).
104 A. Rutherford and D. Duffy, *Journal of Physics: Condensed Matter* **19**, 496201 (2007).
105 S. Zinkle and B. Singh, *Journal of nuclear materials* **199**, 173 (1993).
106 K. Nordlund, S. J. Zinkle, A. E. Sand, F. Granberg, R. S. Averback, R. E. Stoller, T. Suzudo,
L. Malerba, F. Banhart, W. J. Weber, F. Willaime, S. L. Dudarev, and D. Simeone, *Journal
of Nuclear Materials* **512**, 450 (2018).
107 D. Bacon, A. Calder, and F. Gao, *Journal of nuclear materials* **251**, 1 (1997).
108 A. Calder, D. J. Bacon, A. V. Barashev, and Y. N. Osetsky, *Philosophical Magazine* **90**,
863 (2010).
109 M. T. Robinson, *Journal of nuclear materials* **216**, 1 (1994).

110 R. Bullough, M. Hayns, and M. Wood, Journal of Nuclear Materials **90**, 44 (1980).
111 A. Brailsford, R. Bullough, and M. Hayns, Journal of Nuclear Materials **60**, 246 (1976).
112 C. Sun, D. Bufford, Y. Chen, M. A. Kirk, Y. Q. Wang, M. Li, H. Wang, S. A. Maloy, and
X. Zhang, Scientific Reports **4** (2015).
113 R. E. Stoller, Journal of Nuclear Materials - J NUCL MATER **307**, 935 (2002).
114 B. Fu, B. Xu, W. Lai, Y. Yuan, H. Xu, C. Li, Y. Jia, and W. Liu, Journal of Nuclear
Materials **441**, 24 (2013).
115 J. Fikar and R. Schaeublin, Nuclear Instruments and Methods in Physics Research Section
B: Beam Interactions with Materials and Atoms **255**, 27 (2007).
116 C. Broeders and A. Y. Konobeyev, Journal of Nuclear Materials **328**, 197 (2004).
117 C. Klabunde and R. Coltman Jr, Journal of Nuclear Materials **108**, 183 (1982).
118 G. Wallner, M. Anand, L. Greenwood, M. Kirk, W. Mansell, and W. Waschkowski,
Journal of Nuclear Materials **152**, 146 (1988).
119 S. Takamura, T. Aruga, and K. Nakata, Journal of Nuclear Materials **136**, 159 (1985).
120 M. W. Guinan and J. H. Kinney, Journal of Nuclear Materials **108-109**, 95 (1982).
121 F. W. Meyer, P. S. Krstic, H. Hijazi, M. E. Bannister, J. Dadras, C. M. Parish, and H. M.
Meyer, Journal of Physics: Conference Series **488**, 012036 (2014).
122 R. E. Stoller, Journal of nuclear materials **276**, 22 (2000).
123 N. Soneda and T. D. De La Rubia, Philosophical Magazine A **78**, 995 (1998).
124 D. Bacon, A. Calder, F. Gao, V. Kapinos, and S. Wooding, Nuclear Instruments and
Methods in Physics Research Section B: Beam Interactions with Materials and Atoms **102**,
37 (1995).
125 W. Phythian, R. Stoller, A. Foreman, A. Calder, and D. Bacon, Journal of nuclear materials
223, 245 (1995).
126 C. S. Becquart, A. Souidi, and M. Hou, Physical Review B **66** (2002).
127 L. Malerba, Journal of nuclear materials **351**, 28 (2006).
128 K. Nordlund, J. Keinonen, M. Ghaly, and R. S. Averback, Nature **398**, 49 (1999).
129 R. Silsbee, Journal of Applied Physics **28**, 1246 (1957).
130 A. Tenenbaum and N. V. Doan, Philosophical Magazine **35**, 379 (1977).
131 R. S. Nelson, The Philosophical Magazine: A Journal of Theoretical Experimental and
Applied Physics **8**, 693 (1963).
132 R. S. Nelson, M. W. Thompson, and H. Montgomery, Philosophical Magazine **7**, 1385
(1962).
133 R. S. Nelson and M. W. Thompson, Philosophical Magazine **7**, 1425 (1962).
134 H. Ullmaier, P. Ehrhart, P. Jung, and H. Schultz, *Atomic defects in metals*, Vol. 3 (Springer,
1991).
135 S. Fitzgerald, Journal of Micromechanics and Molecular Physics **3**, 1840003 (2018).
136 S. Fitzgerald and D. Nguyen-Manh, Physical review letters **101**, 115504 (2008).
137 D. Nguyen-Manh, A. P. Horsfield, and S. L. Dudarev, Physical Review B **73** (2006).
138 E. Markina, M. Mayer, A. Manhard, and T. Schwarz-Selinger, Journal of Nuclear Materials
463, 329 (2015).
139 H. Schultz, Materials Science and Engineering: A **141**, 149 (1991).
140 Y. Oda, A. M. Ito, A. Takayama, and H. Nakamura, Plasma and Fusion Research **9**,
3401117 (2014).
141 G. Nandipati, W. Setyawan, H. L. Heinisch, K. J. Roche, R. J. Kurtz, and B. D. Wirth,
Journal of Nuclear Materials **462**, 345 (2015).

- 142 C. S. Becquart and C. Domain, Nuclear Instruments and Methods in Physics Research
Section B: Beam Interactions with Materials and Atoms **255**, 23 (2007).
- 143 F. Granberg, J. Byggmästar, and K. Nordlund, The European Physical Journal B **92** (2019).
- 144 G. Was, (2017).
- 145 H. Wang, J.-T. Tian, W. Zhou, X.-F. Chen, B. Bai, and J.-M. Xue, RSC Advances **8**, 14017
(2018).
- 146 L. Ventelon, F. Willaime, C.-C. Fu, M. Heran, and I. Ginoux, Journal of Nuclear Materials
425, 16 (2012).

Figures

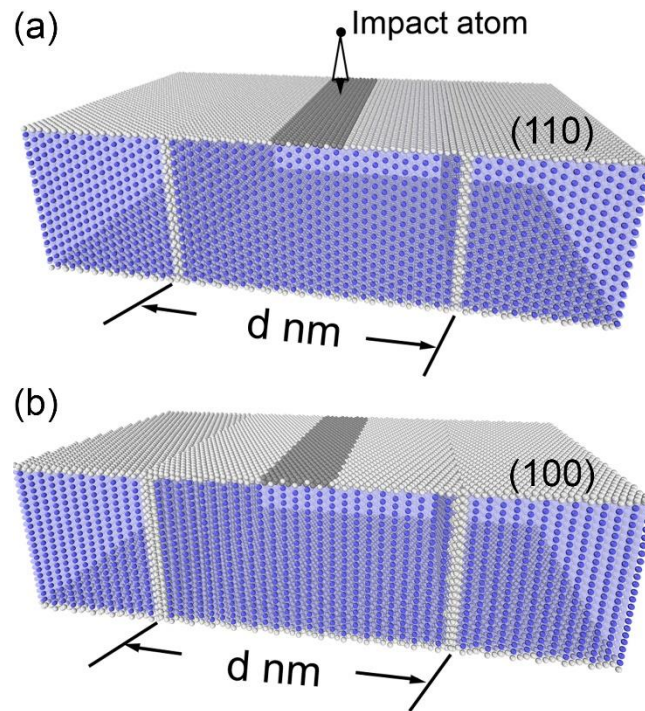


Figure 1. Tungsten nano-bicrystal structures containing (a) the $\Sigma 3 \langle 110 \rangle \{ 112 \}$ grain boundary configuration and (b) the $\Sigma 5 \langle 100 \rangle \{ 130 \}$ grain boundary configuration. The crystallographic orientation of both surfaces is shown with the region over which impact atoms were introduced shaded dark grey. Grain boundary and surface atoms are colored grey and atoms composing the BCC tungsten lattice blue. The grain size, d , was varied between 6 and 12 nm to manipulate cascade interactions with the grain boundaries.

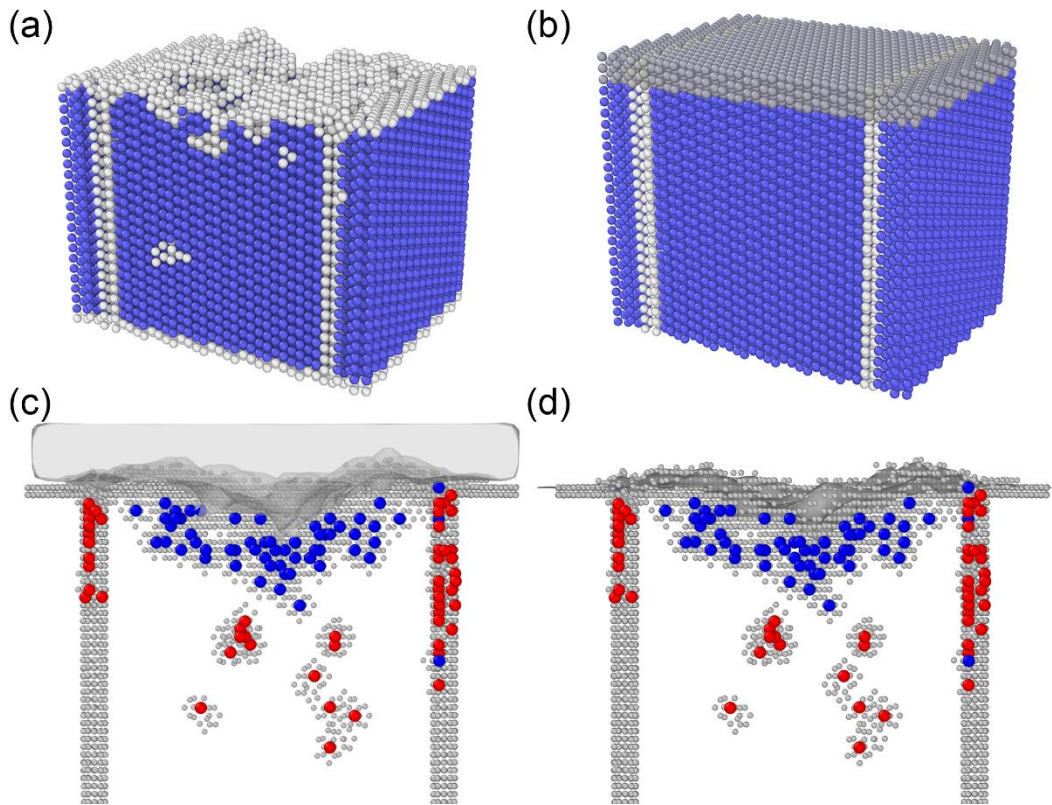


Figure 2. Defect quantification employing an extended reference lattice to account for surface restructuring during the successive impact events. (a) A representative damaged structure after 400 cumulative impacts demonstrating both surface accumulation and the formation of a crater in the primary damage zone. (b) Extended reference lattice where atoms were added to create a 2 nm-thick atomistic cap colored as dark grey. (c) Identification of the surface “vacancy cap”, which is shown removed in (d) with bulk interstitials colored red and vacancies blue.

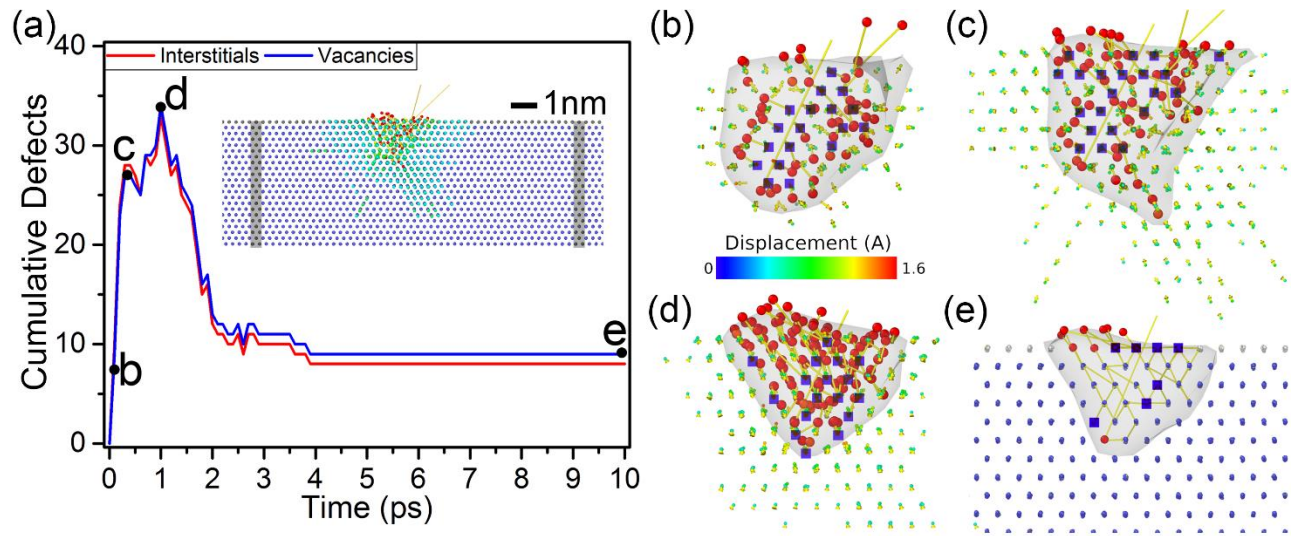


Figure 3. The time evolution of a single collision cascade induced on the (110) surface of the 12 nm grain size tungsten nano-bicrystal containing $\Sigma 3\langle 110 \rangle\{112\}$ grain boundaries. (a) Total number of interstitials and vacancies as a function of time from the initial cascade event with a snapshot of the cascade shown at point c in the inset. Magnified snapshots of the peak damage region at simulation times of (b) 0.2 ps, (c) 0.4 ps, and (d) 1.2 ps, with atoms colored according to the magnitude of their displacement for values > 0.5 Å. Atoms fully displaced from their lattice sites are indexed as large spheres while atoms exhibiting intermediate displacements are shown as smaller spheres. (e) Final defect state at 10 ps after impact. Small spheres indicate the lattice atoms as blue and surface atoms as grey. Large spheres show the defects, red as interstitial and blue as vacancy.

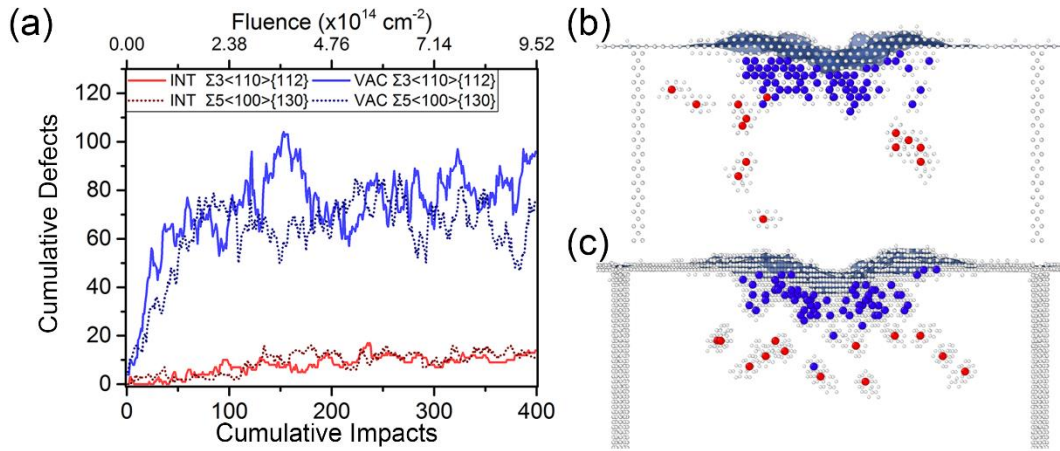


Figure 4. (a) Evolution of interstitials and vacancies during successive displacement cascades in the 12 nm nano-bicrystal containing $\Sigma 3 <110> \{112\}$ (solid lines) and $\Sigma 5 <100> \{130\}$ (dashed lines) grain boundaries. Distributions of vacancies (blue spheres) and interstitials (red spheres) in the (a) $\Sigma 3 <110> \{112\}$ and (b) $\Sigma 5 <100> \{130\}$ structures; grain boundary and surface atoms are colored grey and lattice atoms have been removed for clarity.

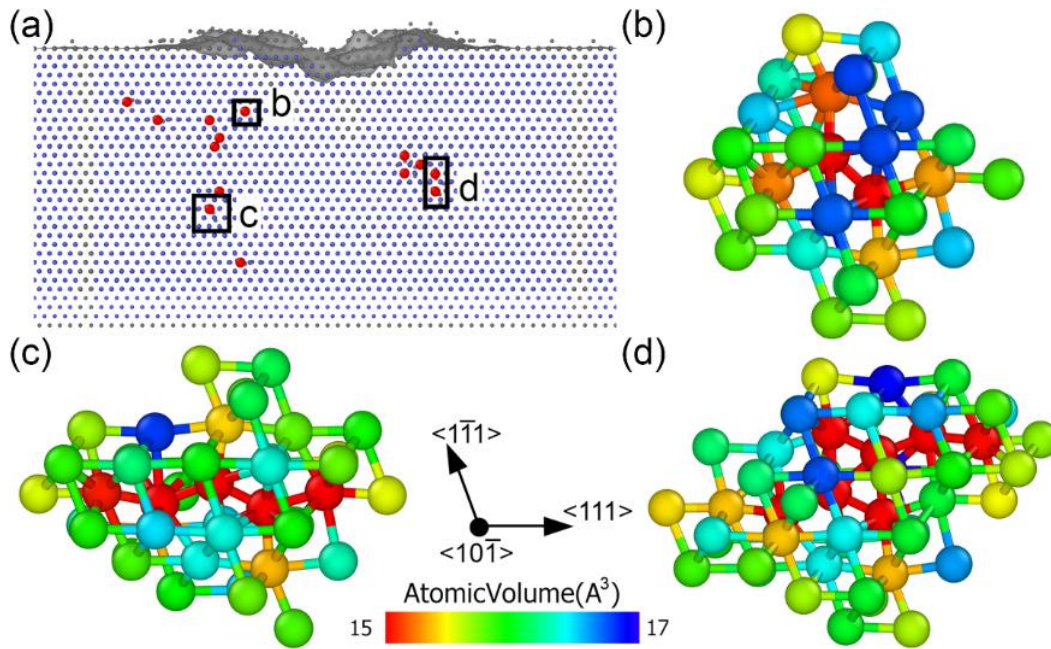


Figure 5. (a) Interstitial distribution in the 12 nm tungsten nano-bicrystal containing $\Sigma 3\langle 110\rangle\{112\}$ grain boundaries with BCC atoms colored blue, grain boundary atoms grey, and interstitials red. Atomic configurations of the interstitials identified in (a) from the modified Wigner-Seitz analysis revealing (b) a $\langle 110\rangle$ dumbbell configuration, (c) a $\langle 111\rangle$ crowdion configuration, and (d) an extended interstitial cluster. In (b-d), the atoms are colored by the atomic volume based on a Voronoi construction.

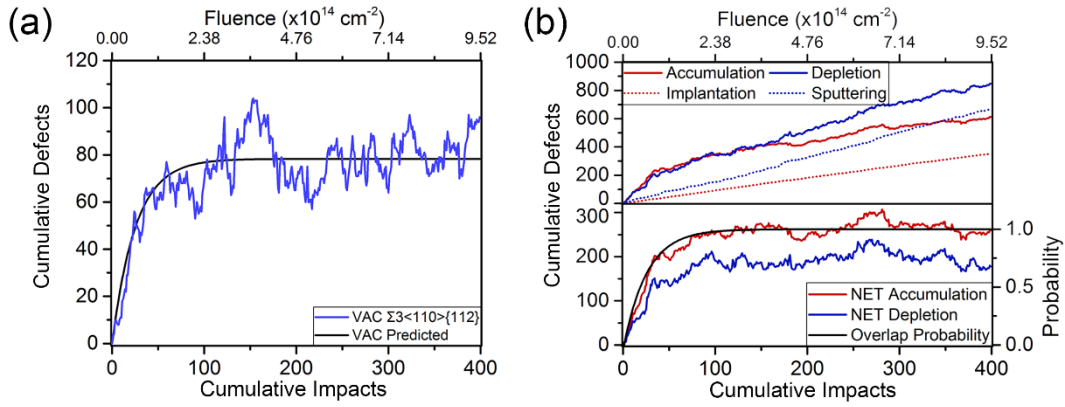


Figure 6. (a) Lattice vacancy accumulation in the 12 nm tungsten nano-bicrystal containing $\Sigma 3\langle 110\rangle\{112\}$ grain boundaries with the predicted vacancy accumulation trend from the cascade overlap probability. (b) Net accumulation and depletion trends (lower panel) as determined from the number of atoms accumulated/depleted on the surface and implanted/sputtered during successive cascades (shown in upper panel). The net accumulation and depletion trends follow the overlap probability also plotted in the lower panel.

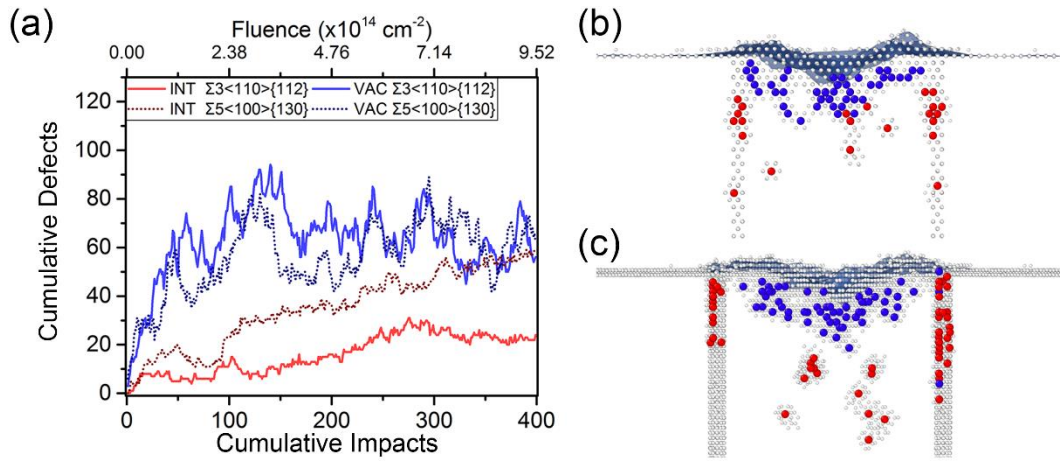


Figure 7. (a) Accumulation of interstitials and vacancies during successive displacement cascades in the 6 nm nano-bicrystal containing $\Sigma 3\langle 110\rangle\{112\}$ (solid lines) and $\Sigma 5\langle 100\rangle\{130\}$ (dashed lines) grain boundaries. Distributions of vacancies (blue spheres) and interstitials (red spheres) in the (a) $\Sigma 3\langle 110\rangle\{112\}$ and (b) $\Sigma 5\langle 100\rangle\{130\}$ structures; grain boundary and surface atoms are colored grey and lattice atoms have been removed for clarity.

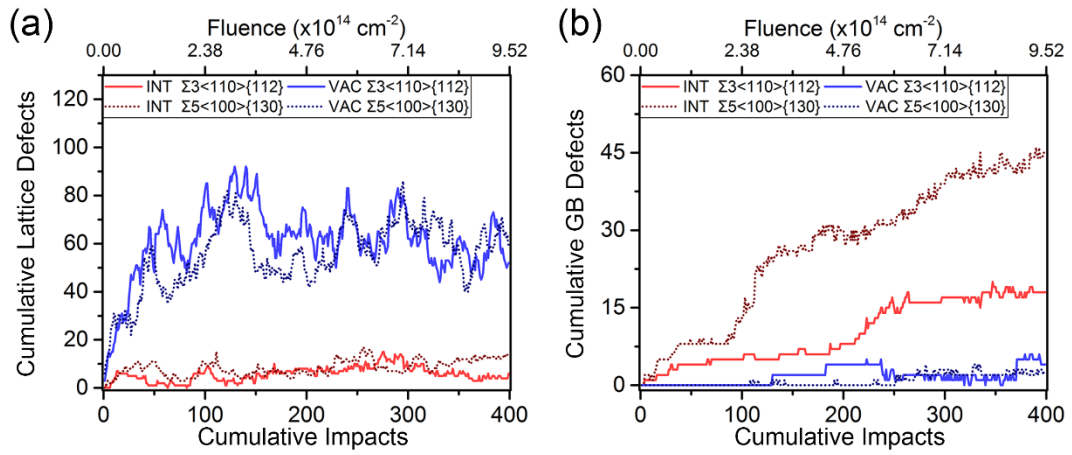


Figure 8. Distribution of point defects within the (a) grain interior containing the BCC lattice and (b) grain boundaries during successive collision cascades in the 6 nm nano-bicrystal. Accumulation of interstitials is largely biased to the grain boundaries whereas vacancy formation is concentrated within the BCC tungsten lattice.

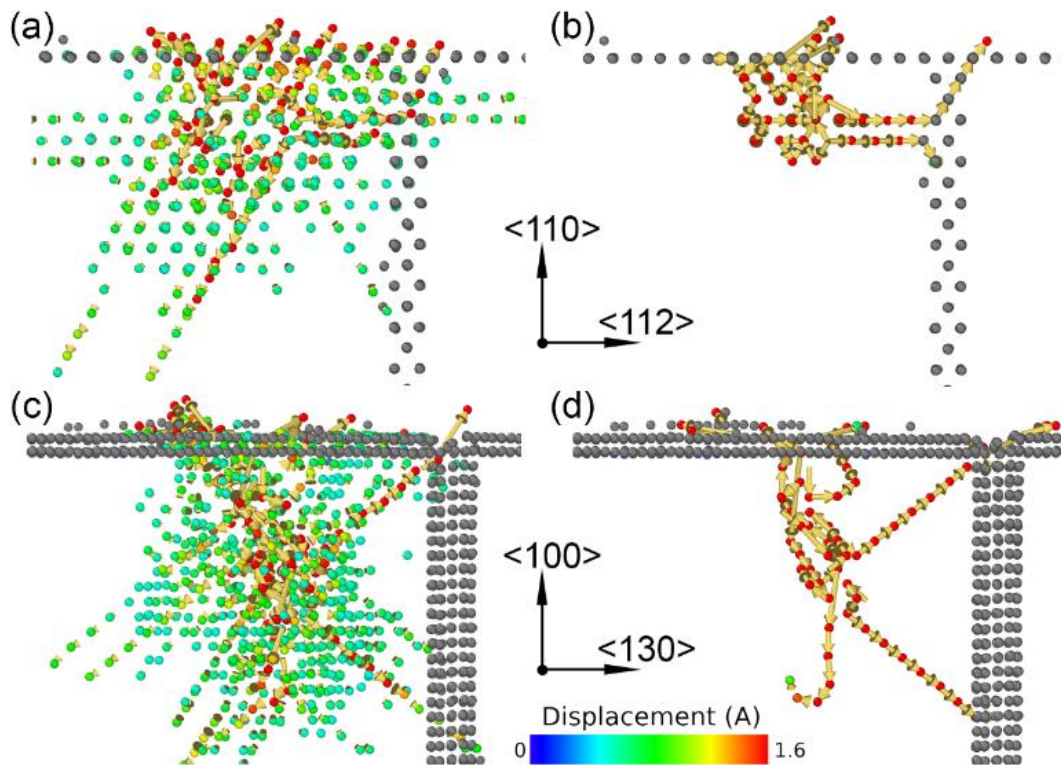


Figure 9. Snapshot of a collision cascade in the 6 nm nano-bicrystal containing $\Sigma 3 \langle 110 \rangle \{ 112 \}$ grain boundaries shown (a) at its peak damage state and (b) after 10 ps of free evolution highlighting the final atomic displacements. Snapshot of a collision cascade in the 6 nm nano-bicrystal containing $\Sigma 5 \langle 100 \rangle \{ 130 \}$ grain boundaries shown (c) at its peak damage state and (d) after 10 ps of free evolution highlighting the final atomic displacements. Atoms within the cascade are colored according to the magnitude of their displacement while grain boundary and surface atoms are grey and all BCC atoms with zero displacement have been removed for clarity.

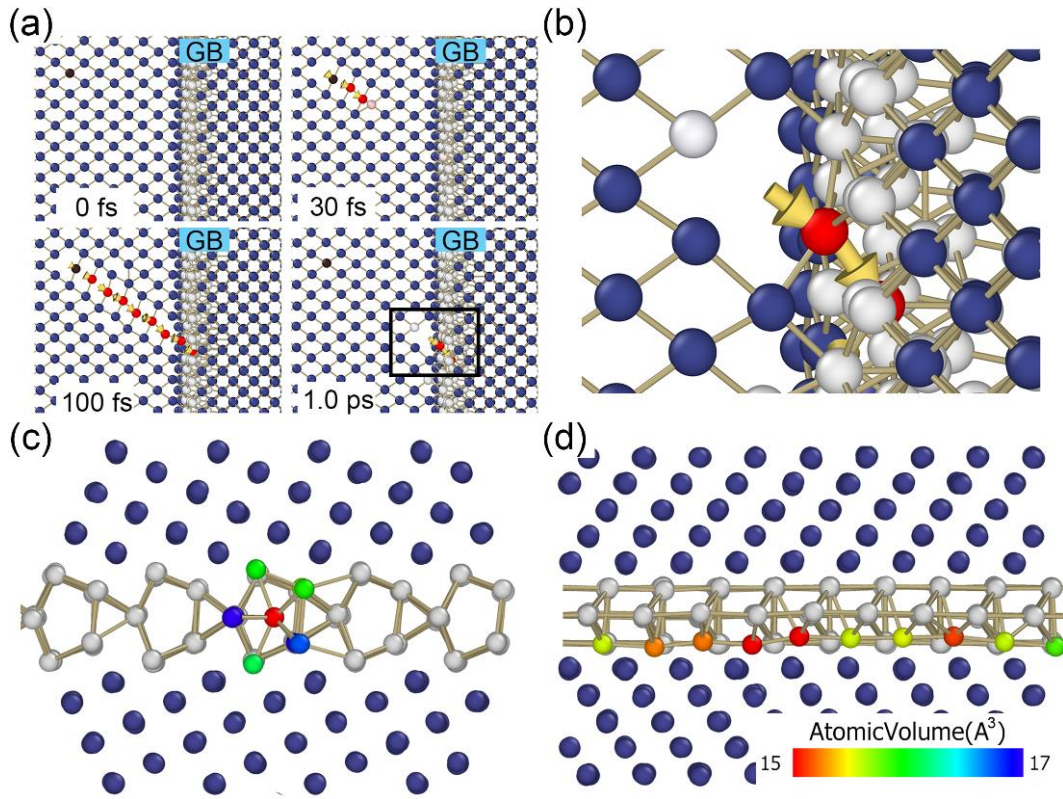


Figure 10. (a) Controlled collision sequence simulation with a 60 eV PKA initiated toward a $\Sigma 5 \langle 100 \rangle \{130\}$ grain boundary along $\langle 111 \rangle$ direction. The collision sequence becomes trapped within the grain boundary plane. (b) Formation of a Frenkel pair near the grain boundary as the collision sequence traverses the interface between the BCC lattice and the grain boundary plane. GB interstitial configurations (c) in the $\Sigma 5$ GB, and (d) in the $\Sigma 3$ GB. Atoms within the interstitial defects are colored according to their atomic volume while atoms occupying the BCC lattice and grain boundary are blue and grey, respectively.

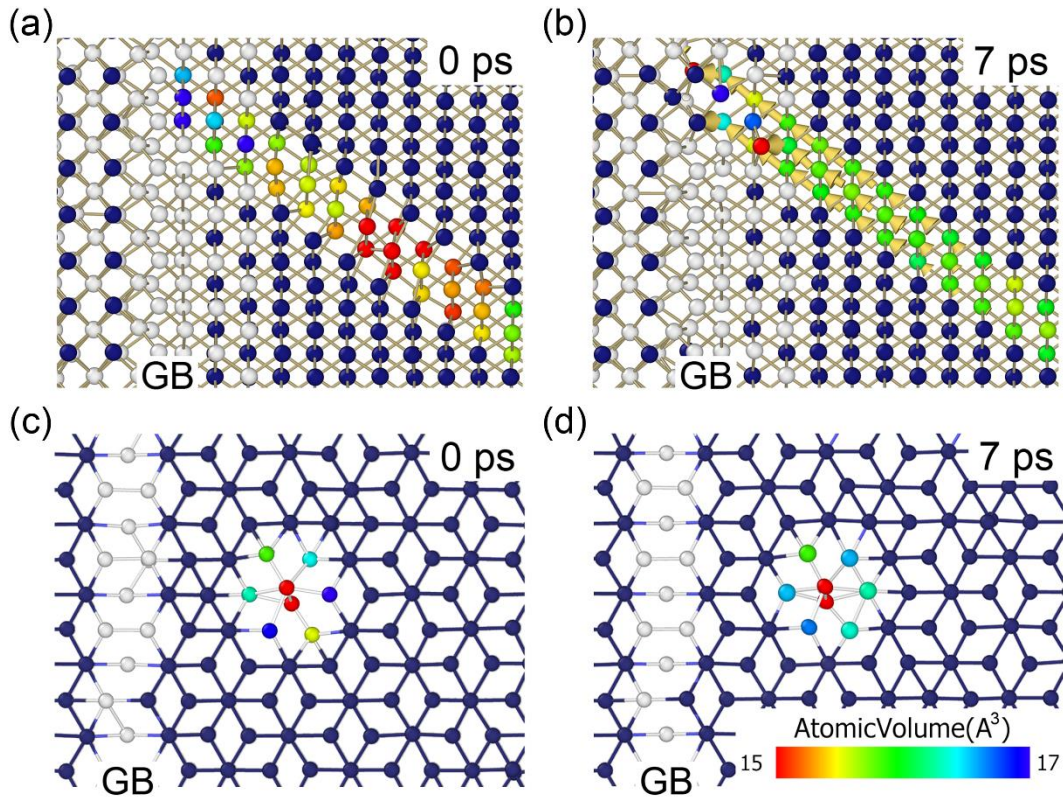


Figure 11. A tri-crowdion in the 6 nm nano-bicrystal adjacent to a $\Sigma 5 \langle 100 \rangle \{ 130 \}$ grain boundary (a) immediately after its formation and (b) at 7 ps when the crowdion migrated to the grain boundary. A crowdion near a $\Sigma 3 \langle 110 \rangle \{ 112 \}$ grain boundary (c) immediately after its formation and (d) 7 ps after where the crowdion has rotated to form a sessile $\langle 110 \rangle$ dumbbell configuration. Atoms within the interstitial defects are colored according to their atomic volume while atoms occupying the BCC lattice and grain boundary are blue and grey, respectively.

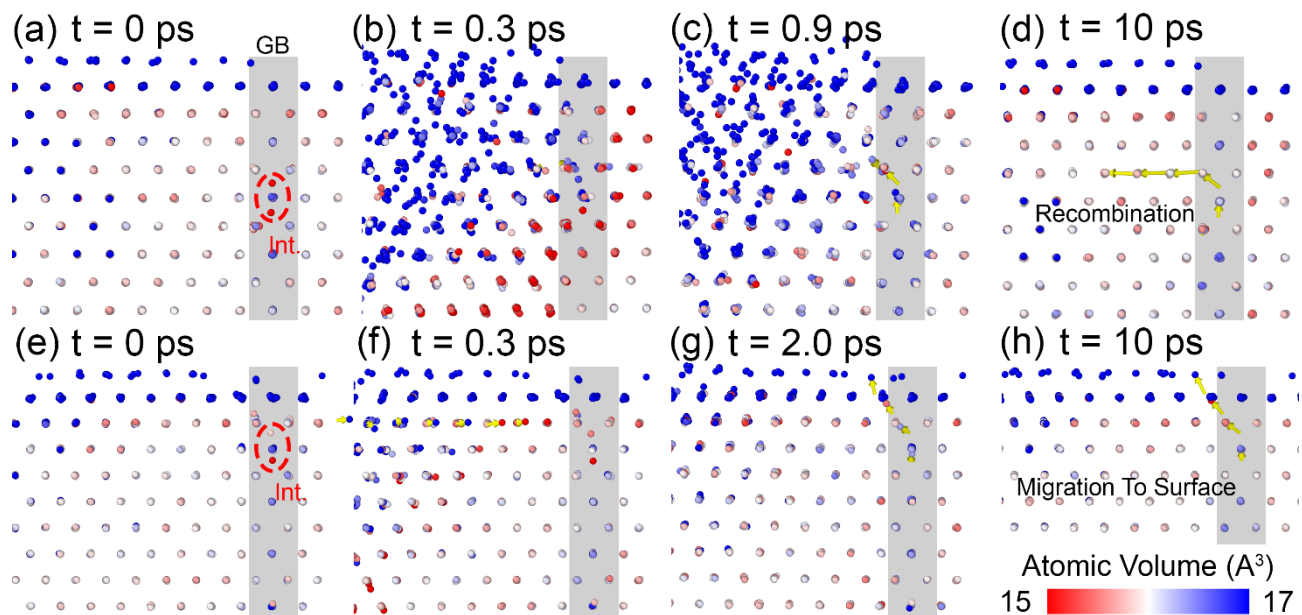


Figure 12. Demonstration of the grain boundary interstitial annihilation through (a-d) recombination with a lattice vacancy during a nearby cascade event and (e-h) migration to the surface due to an intrinsic stress gradient. For each mechanism, figure panels are organized from left-to-right by increasing simulation time, and the yellow arrows indicate the interstitial diffusion path during recombination (upper) and surface migration (lower). All atoms are colored according to their atomic volume with initial interstitial positions identified in (a) and (e).

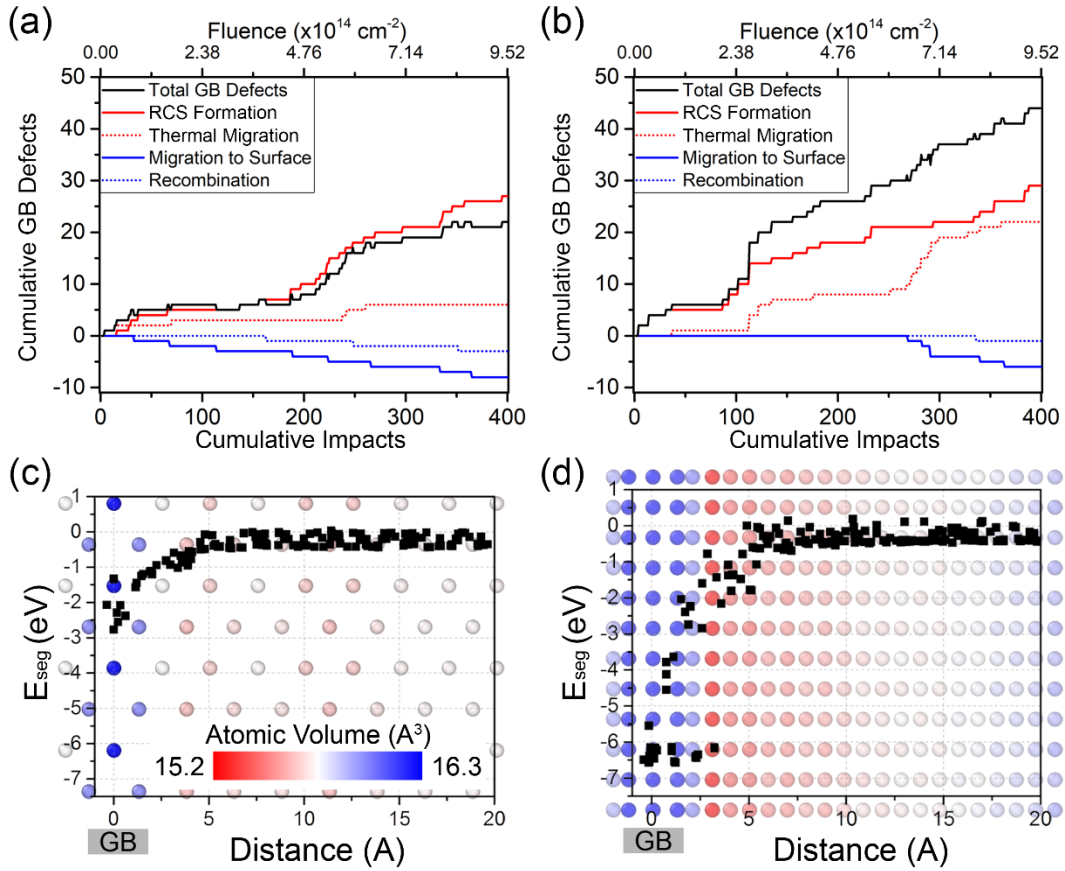


Figure 13. (a-b) Grain boundary defect accumulation trends during successive collision cascades in the 6 nm nano-bicrystal containing (a) $\Sigma 3\langle 110 \rangle \{ 112 \}$ and (b) $\Sigma 5\langle 100 \rangle \{ 130 \}$ grain boundaries. Recognizing the mechanisms of defect accumulation and annihilation, the total defect trends are broken down into contributions from RCS formation (solid red), thermal migration (dashed red), recombination (dashed blue), and migration to the surface (solid blue). The main difference between the configurations derives from the thermal migration contributions to grain boundary defect accumulation driven by different defect segregation energy landscapes. (c-d) Interstitial segregation energy as a function of the distance to the center of the grain boundary plane for the (c) $\Sigma 3\langle 110 \rangle \{ 112 \}$ and (d) $\Sigma 5\langle 100 \rangle \{ 130 \}$ grain boundaries superimposed over the corresponding atomic structures with atoms colored according to atomic volume.

